

Ab initio Modelling of the Early Stages of Precipitation in Al-6000 Alloys

Daniele Giofré^{a,*}, Till Junge^b, W. A. Curtin^b, Michele Ceriotti^a

^aLaboratory of Computational Science and Modeling, Institute of Materials, École Polytechnique Fédérale de Lausanne, 1015 Lausanne, Switzerland

^bLaboratory for Multiscale Mechanics Modeling, Institute of Mechanical Engineering, EPFL, 1015 Lausanne, Switzerland

Abstract

Age hardening induced by the formation of (semi)-coherent precipitate phases is crucial for the processing and final properties of the widely used Al-6000 alloys. Early stages of precipitation are particularly important from the fundamental and technological side, but are still far from being fully understood. Here, an analysis of the energetics of nanometric precipitates of the meta-stable β'' phases is performed, identifying the bulk, elastic strain and interface energies that contribute to the stability of a nucleating cluster. Results show that needle-shape precipitates are unstable to growth even at the smallest size β'' formula unit, i.e. there is no energy barrier to growth. The small differences between different compositions points toward the need for the study of possible precipitate/matrix interface reconstruction. A classical semi-quantitative nucleation theory approach including elastic strain energy captures the trends in precipitate energy versus size and composition. This validates the use of mesoscale models to assess stability and interactions of precipitates. Studies of smaller 3d clusters also show stability relative to the solid solution state, indicating that the early stages of precipitation may be diffusion-limited. Overall, these results demonstrate the important interplay among composition-dependent bulk, interface, and elastic strain energies in determining nanoscale precipitate stability and growth.

*Corresponding author: daniele.giofre@epfl.ch

Keywords: ab initio simulations; aluminum alloys; precipitation; nucleation

1. Introduction

Pure aluminum is lightweight metal that has little strength or resistance to plastic deformation. Alloying aluminum introduces either solutes or the formation of nanometric precipitates that hinder the motion of dislocations, thereby dramatically improving the mechanical properties [1, 2, 3]. A major alloy class used in the automotive industry is the Al-6000 series that contains silicon and magnesium in the range of 0.4–1 wt% with a Si/Mg ratio larger than one. In the initial stages of processing at elevated temperatures, the alloy is a supersaturated solid solution (SSSS), with the solutes randomly dispersed in the Al matrix. After quenching to lower temperatures, the solutes aggregate to form nanometer-sized precipitates (e.g Guinier-Preston (GP) zones, metastable phases, or stable phases, depending on the thermal history). The time evolution of precipitate nucleation and growth is accompanied by a concomitant mechanical strengthening, referred to as age-hardening. Furthermore, precipitation proceeds through a sequence of competing phases that differ in composition, morphology, thermodynamic stability, and kinetics of growth and dissolution, as well as in the contributions to the mechanical properties [4, 5]. Control of the kinetics of age-hardening is crucial for the optimization of the final mechanical properties.

In commercial 6000-series Al alloys, precipitation commences at room temperature shortly after quenching, and this “natural aging” is undesirable. Subsequent “artificial aging” at elevated temperature is then used to achieve the desired precipitate type(s) and sizes. The most effective hardening conditions are obtained in the early stages of precipitation, where fully-coherent GP zones coexist with the semi-coherent β'' phase [6], which forms needle-shaped precipitates 200-1000 Å in length and ≈ 60 Å in diameter [7, 8]. High-resolution electron microscopy and quantitative electron diffraction [9, 7] studies have revealed that the β'' phase is characterized by a Mg/Si ratio close to 1 but with

different possible stoichiometries that include Mg_5Si_6 , $\text{Mg}_4\text{Al}_3\text{Si}_4$, $\text{Mg}_5\text{Al}_2\text{Si}_4$. Recent first-principles calculations have predicted that the latter composition is the most stable[10]. While considerable progress has been made in understanding the structure of the β'' phase, and the behavior of the SSSS [11], little is known on the early stages of the aging mechanism, and in particular on the thermodynamics of the initial clustering of solutes to form the precipitate [1, 2, 12, 9]. Such knowledge is crucial to gain better control over the balance between natural and artificial aging.

In the present work we study the energetics of nanoscale precipitates using *ab initio* electronic structure methods so as to identify the different contributions to the thermodynamic in-situ precipitation energetics. We compute the energy contributions due to the precipitate formation energy, the precipitate/matrix interface energies, and the elastic energy due to lattice and elastic mismatch between precipitate and matrix. We show that these contributions semi-quantitatively capture the total energy of in-situ precipitates as a function of precipitate size. Our results demonstrate that – down to the size of a single formula unit of the β'' phase, fully encapsulated in the Al matrix – the precipitate growth process can proceed without energetic barriers. Since the nucleation process of the β'' phase has nearly zero barrier, control of precipitation kinetics should focus on aggregates of atoms of even smaller size.

The remainder of this paper is organized as follows. In Section 2 we describe the details of our *ab initio* simulations. In Section 3 we report a few benchmarks on the bulk properties of the different stoichiometries proposed for the β'' phases. In Section 4 we discuss a classical-nucleation-theory (CNT) model of precipitate stability, including surface energies and the continuum elasticity model of lattice mismatch relaxation, and compare with DFT results for needle-like precipitates. In Section 5 we present *ab initio* simulations of fully-encapsulated clusters. We finally draw conclusions.

2. Computational details

Density functional theory (DFT) has been shown to provide reliable energetics for aluminum and its alloys [10, 13, 14, 11]. We have used self-consistent DFT as implemented in the Quantum ESPRESSO (QE) package[15]. We used a gradient corrected exchange and correlation energy functional (PBE)[16], together with a plane-waves expansion of Kohn-Sham orbitals and electronic density, using ultra-soft pseudopotentials for all the elements involved [17, 18, 19]. All calculations were performed with a k -point sampling of the Brillouin zone using a grid density of $\approx 5 \cdot 10^{-6} \text{ \AA}^{-3}$ and a Monkhorst-Pack mesh[20]. The plane-wave cut-off energy was chosen to be 35 (280) Ry for the wavefunction (the charge density) when evaluating the energetics of defects (i.e. for computing formation, surface, and precipitation energies). Test calculations performed at larger cutoffs showed that these parameters are sufficient to converge the atomization energy of Al at a level of 0.3 meV/atom. Cutoffs were increased to 50 (400) Ry so as to converge the value of the elastic constants to an error below 1 GPa. Comparison with previous literature results, where available, will be presented below.

3. Bulk properties of matrix and precipitate phases

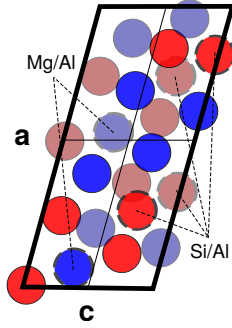
Bulk properties (lattice structure, lattice constants, elastic constants) of Al and the various β'' -precipitates studied here have been previously computed in the literature. Here, we present our results as a means of benchmarking our methods, verifying literature results, and most importantly obtaining reference values that are fully consistent with our computational details – which is crucial to evaluate the energy differences that determine surface and defect energies.

For bulk *fcc* Al, we computed the lattice parameter to be 4.057 Å, in excellent agreement with the experimental value and with previous modelling using the same functional [21, 22]. These lattice parameters are used throughout our study to build supercells representing the Al matrix. All of the β'' phases we consider can be described by a monoclinic cell containing two formula units

(f.u.). We consider three compositions, Mg_5Si_6 , $\text{Mg}_5\text{Al}_2\text{Si}_4$ and $\text{Mg}_4\text{Al}_3\text{Si}_4$, as shown in Figure 1. We computed the crystal structures of these β'' -precipitates starting from the geometries proposed in previous works [7]. The equilibrium lattice parameters and monoclinic angles are shown in Table 1, and agree well with existing literature [4]. Inside the Al matrix, the main crystallographic directions (lattice vectors) of the precipitate are aligned with those in the *fcc* lattice of aluminum as follows:

$$[100]_{\beta''} \parallel [203]_{\text{Al}} \quad [010]_{\beta''} \parallel [010]_{\text{Al}} \quad [001]_{\beta''} \parallel [\bar{3}01]_{\text{Al}}. \quad (1)$$

The ideal monoclinic unit cell can be deformed, relative to the fully relaxed structures, to substitute for 22 Al atoms. The corresponding lattice vectors and lattice constants of the 22-atom Al are shown Table 1. The difference between the ideal monoclinic unit cell and the 22-atom Al unit cell uniquely determines the misfit strain tensor of the precipitate in the Al lattice, which will be used below to determine the corresponding elastic energy of precipitates in the matrix.



Composition	a [\AA]	b [\AA]	c [\AA]	β [$^\circ$]
Mg_5Si_6	15.14	4.08	6.93	109.9
$\text{Mg}_5\text{Al}_2\text{Si}_4$	15.33	4.05	6.84	106.0
$\text{Mg}_4\text{Al}_3\text{Si}_4$	15.13	4.12	6.65	106.6
Matrix[7]	14.63	4.06	6.41	105.3

Table 1: (Left) A view along the \mathbf{b} lattice vector of the monoclinic unit cell of β'' phases. The red and blue circles represent Si and Mg atoms, respectively, while the different shading indicates the position of the atoms at a height of zero and $|\mathbf{b}|/2$ along the \mathbf{b} vector. Circles with dashed outline indicate the atoms that can be substituted to obtain the three β'' stoichiometries (that is, Mg_5Si_6 , $\text{Mg}_5\text{Al}_2\text{Si}_4$ and $\text{Mg}_4\text{Al}_3\text{Si}_4$)[10]. (Right) The fully-relaxed bulk lattice parameters of the β'' phases, compared with those that correspond to an ideal embedding within the Al matrix.

We computed the elastic constants of all bulk phases by evaluating the

[GPa]	C_{11}	C_{22}	C_{33}	C_{44}	C_{55}	C_{66}	
Al	106.1 (114.3)			31.9 (31.6)			
Mg ₅ Si ₆	98.4	84.6	88.0	21.9	29.1	51.2	
Mg ₅ Al ₂ Si ₄	107.1	94.7	99.1	26.9	36.3	49.4	
Mg ₄ Al ₃ Si ₄	106.7	96.5	97.1	25.9	35.6	46.3	
	C_{12}	C_{13}	C_{23}	C_{15}	C_{25}	C_{35}	C_{46}
	55.9 (61.9)			0.			
	50.0	47.7	45.7	8.2	5.8	5.4	-10.1
	40.3	45.6	43.0	-13.1	4.3	11.9	5.4
	46.5	48.0	48.8	9.3	5.7	9.3	6.3

Table 2: Elastic constants obtained by a linear fit of ab-initio stress tensors for small cell deformations. The values in parentheses are the experimental ones, extrapolated to 0K.[24]

stresses generated by small displacements of the unit cell around the equilibrium structure. A suitable set of displacements was used, and the stresses were then modelled as a linear function of the displacements to obtain the elastic constants [23]. The elastic constants for bulk Al and for the three β'' phases studied here are shown in Table 2, and were computed according to a reference system consistent with the Al matrix, as shown in Fig. 2. Our values are in good agreement with available experimental values [24] and previous computations [25, 10, 26].

In order to define a reference state for the thermodynamics of the precipitates we define the solid solution energies as

$$E_{\text{Al}}^{\text{ss}} = E_{\text{Al}_M}^{\text{tot}} / M \quad (2)$$

$$E_x^{\text{ss}} = E_{\text{Al}_{M-1}(x)}^{\text{tot}} - (M-1)E_{\text{Al}}^{\text{ss}}, \quad (3)$$

for $x = \text{Si, Mg}$. Here, $E_{\text{Al}_M}^{\text{tot}}$ and $E_{\text{Al}_{M-1}(x)}^{\text{tot}}$ are the total energies of a bulk-Al supercell containing M Al atoms and $(M-1)$ Al atoms and 1 atom of $x = \text{Si, Mg}$, respectively. The energy $E_{\text{Al}_{M-1}(x)}^{\text{tot}}$ is computed using a single solute in a 4x4x4 unit periodic cell with the cell volume held fixed. The cell develops a small

	E_{form} [eV/f.u.]	γ [meV/Å ²] [mJ/m ²]			E_{strain} [meV/f.u.] (size: f.u./l.u.)			
		A	B	C	dilute	$N : 1$	4	16
					1×1	1×1	2×2	4×4
					<i>96×96</i>	<i>5×5</i>	<i>7×7</i>	<i>12×12</i>
Mg ₅ Si ₆	-2.607	8.36 <i>134</i>	21.1 <i>338</i>	2.69 <i>43.1</i>	140	171	203	223
Mg ₅ Al ₂ Si ₄	-2.769	11.8 <i>189</i>	23.5 <i>376</i>	9.11 <i>146</i>	128	161	198	223
Mg ₄ Al ₃ Si ₄	-2.366	10.1 <i>162</i>	20.4 <i>327</i>	8.24 <i>132</i>	74	89	106	117

Table 3: Bulk, strain, and surface-energy terms computed for the three stoichiometries of the β'' phase which we considered in this study. The elastic strain energy E_{strain} has been computed for the dilute case and for the three periodic cases with varying numbers of formula units (N). The precipitate size is reported in formula units (f.u.) and the matrix size in fcc lattice unit cells (l.u.).

pressure due to the misfit volume of the solute, but this contribution to the energy is negligible for the large cell size used.

The formation energy for a precipitate can then be defined as the total energy of a precipitate formula unit relative to that of the total energies of the precipitate atoms in the solid solution state. Thus, the formation energy is

$$E_{form} = \frac{1}{2} E_{\beta''}^{tot} - \sum_{x=Al, Si, Mg} n_x \cdot E_x^{ss}, \quad (4)$$

where $E_{\beta''}^{tot}$ is the (DFT) total energy of a fully-relaxed unit cell of the β'' phase containing 22 atoms (2 formula units), n_x is the number of atoms of element x in one formula unit, and E_x^{ss} is the energy of solute x in the (dilute) solid solution state. Knowing all the terms in eq. 4, we can compute the formation energies of the three proposed β'' -phase compositions as shown in Table 3). The precipitates are strongly favorable, with negative formation energies in excess of -2eV/f.u., or greater than -0.2 eV/atom on average. Precipitate formation is thus thermodynamically highly preferable relative to the solid solution state.

4. In-situ precipitates

Bulk properties provide important information on the thermodynamic driving forces for precipitation, but are incomplete for understanding in-situ precipitation nucleation and growth. The system of precipitate plus matrix has additional energetic contributions from the precipitate/matrix interfaces, precipitate/matrix lattice and elastic constant mismatches that give rise to elastic energies when the precipitate is coherent, and precipitate/matrix edge and corner energies. All of these additional contributions determine the total thermodynamic driving force for precipitate growth as a function of precipitate size, shape, and density. While not addressed here, the elastic interactions between precipitates at finite densities also influences their spatial arrangement and orientation [27, 28, 29].

We thus need to predict the size, shape, and energy of a critical precipitate nucleus. At some critical precipitate size, the precipitate becomes thermodynamically unstable to further growth, i.e. increasing size leads to decreasing total energy. Below the critical precipitate size, the precipitate is unstable and should re-dissolve in the solid solution. Here, we take a model based on classical nucleation theory (CNT) to assess the precipitate stability as a function of size, shape and density (which influences the elastic energy). In this analysis, we ignore edge and corner energies. Also assuming, for the moment, a low density of precipitates, the total energy of a precipitate containing N formula units, relative to the SSSS, can be written as

$$E_{prec}(N) = NE_{form} + NE_{strain} + E_{surf}(N). \quad (5)$$

There are two new terms in Eq. 5. First, there is the elastic strain energy E_{strain} due to the lattice and elastic mismatch between the precipitate and the Al-matrix per β'' formula unit for a single precipitate in an infinite matrix (the dilute limit). Second, there is the surface (interface) energy E_{surf} of the precipitate, which will depend on both the size and the shape of the nucleus. In order to evaluate the precipitation energy, we first obtain quantitative values

for the strain and interface energies. Then, we will make predictions for the thermodynamics in the dilute limit. Finally, we will perform DFT studies of in-situ precipitates and compare the DFT energies versus the CNT model, adapted to the geometry of the DFT supercells.

4.1. Interface energies for β'' precipitates

Based on TEM analyses [30, 9, 5], and the correspondence between β'' structure and the closely-related 22-atom Al unit that accommodates one precipitate unit cell, we study three interface orientations as shown in Figure 1. The orientations are denoted A $\equiv (103)_{\text{Al}} \equiv (100)_{\beta''}$, B $\equiv (010)_{\text{Al}} \equiv (010)_{\beta''}$, and C $\equiv (\bar{3}02)_{\text{Al}} \equiv (001)_{\beta''}$. Given the relatively complex structure of the β'' phase, there are many possible ways to terminate the precipitate. Previous computational studies of the β'' -Mg₅Si₆/ α -Al interface have found that the associated surface energies can change significantly between different choices [31]. To compare with previous studies of finite-size precipitates, we chose the interfaces used in Ref. 10. Figure 1 shows only one monoclinic unit cell of the precipitate and one for the matrix for Mg₅Al₂Si₄ but all three compositions were studied, and simulations were performed with much larger supercells of sizes $4\beta'' + 4\text{Al}$ unit cells for the A orientation, $6\beta'' + 6\text{Al}$ unit cells for the B orientation, and $6\beta'' + 6\text{Al}$ unit cells for the C orientation.

Since the precipitate and matrix have a structural mismatch, the total energy computed in a given simulation cell includes an elastic deformation energy. This energy must be computed independently and subtracted from the total energy obtained in the interface simulation to estimate the specific interface energy $\gamma_{\Lambda=A,B,C}$. First, we compute the energy per formula unit of the partially-relaxed β'' phase. For each interface orientation, we define $E_{\Lambda}^{\beta''}$ as the energy per formula unit of a β'' cell that is fully coherent with the Al matrix in the Λ plane, and relaxed in the orthogonal direction. We then prepared an interface between the Al matrix and the β'' phase, once again fixing the dimensions parallel to the interface to be fully coherent with the matrix, and relaxing it in the orthogonal direction. The interface energy can then be obtained from the

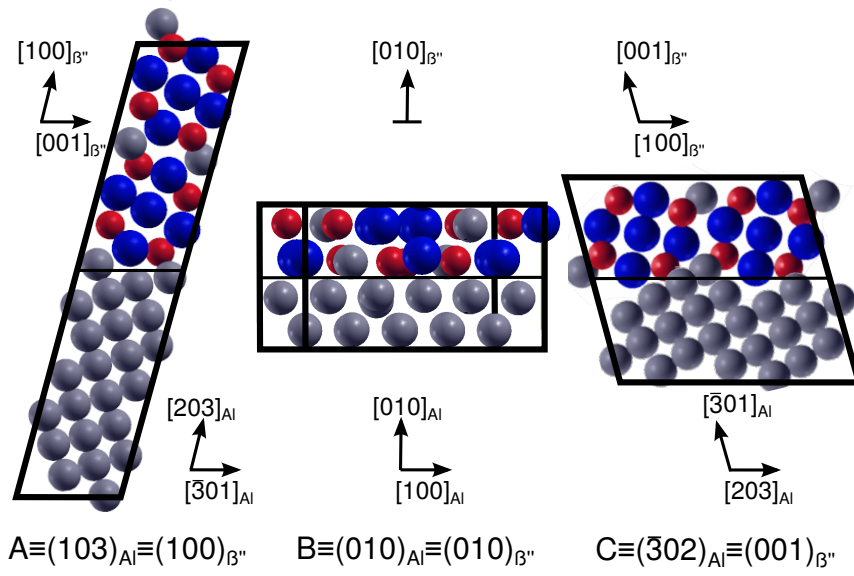


Figure 1: We considered three orientations for the interfaces the between β'' precipitate and the Al matrix: the A orientation (left), the B orientation (center), and the C orientation (right). While we chose to represent only the $Mg_5Al_2Si_4$ phase, for simplicity, the other two compositions can be obtained by performing the substitutions indicated in Tab. 1.

total energy of this supercell E_{Λ}^{sc} as

$$\gamma_{\Lambda=A,B,C} = \frac{\left(E_{\Lambda}^{sc} - n_{Al}E_{Al}^{SS} - n_{\beta''}E_{\Lambda}^{\beta''}\right)}{2S_{supercell}^{\Lambda}}, \quad (6)$$

where $S_{supercell}^{\Lambda}$ is the cross-section of the simulation supercell corresponding to the orientation of the interface, n_{Al} is the number of Al atoms in the matrix, and $n_{\beta''}$ is the number of β'' formula units inside the supercell. The computed surface energies for each orientation are shown in Table 3.

As previously noted [31], the B surface energy is relatively large but the anisotropy is not sufficient to fully explain the observed needle-shaped habit of the precipitates. Given the large range of values observed for different terminations [31], a change in composition or some degree of interface reconstruction may significantly lower the energies of the A and C interfaces, leading to larger anisotropy. For instance, we obtain a considerably lower surface energy for the C interface in Mg_5Si_6 than any of the values reported in Ref. 31. For this specific case – that is associated with a relatively large mismatch in the unit cells between the β'' phase and the matrix – we observe significant relaxation of atoms at the interface, extending for several layers in the bulk, that was probably not captured fully in the smaller supercells¹ used in Ref. 31. The issue of interface energies of β'' phases in Al thus merits further study.

4.2. Elastic strain energies of needle-like β'' precipitates

During the aging process, β'' precipitates show a strongly anisotropic habit, extending along the $b \equiv [010]$ direction forming needle-like semi-coherent particles. The lattice mismatch between Al and β'' along the crystallographic b direction is also quite small. For this reason, two-dimensional slices along the a, c axes of the precipitate capture the main contributions to the energetics of large precipitates, and have already been studied to characterize both the

¹Calculations in Ref. 31 used 44+44 atoms supercells, while our calculations for the C interface contained 132+132 atoms. We verified that when using a supercell with 66+66 atoms the surface energy for $Mg_5Si_6(C)$ increased to 63 mJ/m², getting closer to previous results.

energetics and elastic deformation of the matrix in this regime [32, 31]. To compute the magnitude of the elastic strain energy contribution for such a two-dimensional slice, we will use anisotropic continuum elasticity. The boundary value problem is formulated to correspond to the direct DFT studies below. We study a periodic two-dimensional plane-strain problem with a fully three-dimensional eigenstrain within the precipitate due to the misfit between the precipitate and the matrix. Figure 2 shows a schematic of the geometry with the relevant coordinate axes.

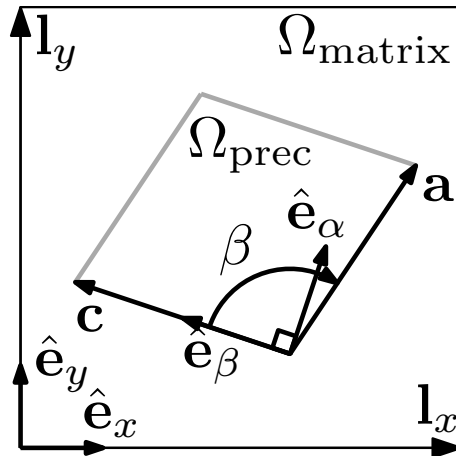


Figure 2: Schematic of the computational domain and definition of frames of reference. The directions of the vectors \vec{c} and \vec{a} are drawn as defined by (1), vectors \vec{b} and \hat{e}_z point out of the paper (not depicted). The global frame of reference is $\hat{e}_x-\hat{e}_y-\hat{e}_z$ while the elastic constants listed in Table 2 are measured in the material frame $\hat{e}_\alpha-\hat{e}_\beta-\hat{e}_z$.

The Al matrix Ω_{matrix} is modeled as linearly elastic,

$$\boldsymbol{\sigma} = \mathbf{C}_{matrix}\boldsymbol{\epsilon} \quad \text{in } \Omega_{matrix}, \quad (7)$$

where $\boldsymbol{\sigma}$ and $\boldsymbol{\epsilon}$ are the Cauchy stress and strain tensors and \mathbf{C}_{matrix} is the anisotropic fourth-order stiffness tensor of the matrix expressed in the global frame of reference $\hat{e}_x-\hat{e}_y-\hat{e}_z$ aligned with the cubic lattice vectors of the pure aluminum matrix. The precipitate Ω_{prec} is also linearly elastic, but with an additional eigenstrain $\bar{\boldsymbol{\epsilon}}$ relative to the reference Al lattice that accounts for the

size and shape misfit of the precipitate,

$$\boldsymbol{\sigma} = \mathbf{C}_{prec}(\boldsymbol{\epsilon} - \bar{\boldsymbol{\epsilon}}) \quad \text{in } \Omega_{prec}. \quad (8)$$

Determination of the eigenstrain $\bar{\boldsymbol{\epsilon}}$ and the rotation of the stiffness tensor \mathbf{C}_{prec} into the global frame of reference are described in the Appendix A.

As a plane-strain problem, there is zero out-of-plane displacement $u_z = 0$. Therefore the total strain tensor has $\epsilon_{xz} = \epsilon_{yz} = \epsilon_{zz} = 0$. The eigenstrain $\bar{\boldsymbol{\epsilon}}$ retains these components, however, so that the effects of the mismatch in the z direction are included. We impose periodic Dirichlet boundary conditions on the displacement \vec{u} in the horizontal and vertical directions

$$\vec{u}(\vec{x}) = \vec{u}(\vec{x} + n\vec{l}_x + m\vec{l}_y), \quad n, m \in \mathbb{Z}, \quad \forall \vec{x} \in \partial\Omega, \quad (9)$$

where \vec{l}_x and \vec{l}_y are the vectors linking the bottom left corner to the bottom right and the top left, respectively. We fix an arbitrary point $u(\vec{x}_p) = 0$ to exclude solid body motion. The static equilibrium stress and strain fields throughout the body are then determined by solving the standard equilibrium equation $\nabla \cdot \boldsymbol{\sigma} = \vec{0}$. With the computed stress field, the strain fields are obtained from the constitutive models above and the elastic strain energy (per unit length in the out-of-plane direction) E_{strain} is then computed as

$$E_{strain} = \frac{1}{2} \left(\int_{\Omega_{matrix}} \boldsymbol{\epsilon} \mathbf{C}_{matrix} \boldsymbol{\epsilon} \, d\Omega + \int_{\Omega_{prec}} (\boldsymbol{\epsilon} - \bar{\boldsymbol{\epsilon}}) \mathbf{C}_{prec} (\boldsymbol{\epsilon} - \bar{\boldsymbol{\epsilon}}) \, d\Omega \right) \quad (10)$$

Note that the energy per unit length is independent of absolute model size and so the energy only depends on the size of the precipitate relative to the size of the computational cell, or equivalently on the area fraction (equal to the volume fraction) of the precipitate.

The boundary value problem is solved using the finite-element method (see Appendix B). Note that, although the problem is nominally two-dimensional (plane-strain), the evaluation of the elastic strain energy remains fully three-dimensional due to the eigenstrain $\bar{\boldsymbol{\epsilon}}$. Using the above implementation, we first computed the elastic strain energy per formula unit in the dilute limit where interactions among precipitates are negligible. This is done by using one

formula unit in a cell of 96 x 96 fcc unit cells, and the results are shown as the “dilute” limit in Table 3. The elastic energies are small compared to the chemical energies, but are not small compared to differences in energies among precipitate compositions.

4.3. *In-situ energetics of dilute needle-like β'' precipitates*

Having evaluated separately the bulk, surface, and elastic relaxation energies for a needle-like precipitate of the β'' phases, we can then proceed to estimate the overall energetics of a nucleus. Assuming for simplicity the surface area of the interfaces to be that of the matrix-coherent unit cell (that is 26.02 Å² for each formula unit along the A facets, and 29.7 Å² for each formula unit along the C facets) we find that a needle-like precipitate with a cross-section of a single formula has already a negative formation energy. Considering the elastic energy associated with the infinite-dilution limit, one obtains $E_{prec} = -1.872$ eV for 1 f.u. of Mg₅Si₆, $E_{prec} = -1.486$ eV/f.u. for Mg₅Al₂Si₄, and $E_{prec} = -1.278$ eV/f.u. for Mg₄Al₃Si₄. The formation of the β'' phases starting from the SSS is so exoenergetic that needle-like precipitates can form without overcoming a free energy barrier. Due to the much lower surface energy for the C interface, in the small-precipitate limit Mg₅Si₆ forms the most stable precipitate. In the limit of macroscopic precipitates, the energy per f.u. tends to the precipitation energy plus the dilute-limit elastic contribution, given as $E_{\infty} = -2.467$ eV/f.u. for Mg₅Si₆, $E_{\infty} = -2.651$ eV/f.u. for Mg₅Al₂Si₄, and $E_{\infty} = -2.292$ eV/f.u. for Mg₄Al₃Si₄. Thus, Mg₅Al₂Si₄ is predicted to be the most stable form in the large-precipitate limit. The elastic strain energy does not change the order of stability but does narrow the energy difference between the most and least stable down to 0.35 eV/f.u. or 0.032 eV/atom

4.4. *DFT of needle-shaped precipitates and comparison to CNT model*

The CNT model of precipitate energetics we have introduced in Eq. 5, including self-consistent elasticity terms, could be very useful to examine the interaction between growing precipitates. In order to assess its accuracy, we use

the same needle-like geometry to evaluate the energetics of precipitates using DFT, and perform a comparison with the results of the model. To be consistent with the definition of formation energies used above, we define the precipitation energy using the SSSS as reference, i.e.

$$E_{prec}(N) = E_{sys}^{tot}(N) - M E_{Al}^{ss} - N \sum_{x=Si, Mg, Al} n_x \cdot E_x^{ss}, \quad (11)$$

where M is the number of Al atoms in the matrix for a give simulation supercell, and n_x and E_x^{ss} indicate the β'' composition and the solid-solution energy for Al, Si and Mg, as in Eq. (4).

To benchmark the model across different precipitate sizes, we study three systems whose cross-section contains 1, 4, and 16 formula units of precipitate in an equiaxed geometry. These precipitates are embedded in an Al matrix supercells of sizes $(a \times b \times c)$ $5 \times 1 \times 5$, $7 \times 1 \times 7$, and $12 \times 1 \times 12$ *fcc* unit cells, respectively, as shown in Fig. 4(a) for the supercell containing 16 f.u. of the β'' phase).

As noted above, the elastic energy depends on the precipitate density or cell geometry. The DFT cells are not in the dilute limit. Therefore, for comparison to the DFT energies, the CNT model is modified to account for the elastic energy changes in the non-dilute limit as

$$E_{prec}(N) = N E_{form} + N E_{strain}(N, V) + E_{surf}(N), \quad (12)$$

where $E_{strain}(N, V)$ is the elastic strain energy per formula unit in a supercell of volume V containing a precipitate of size N formula units. Elasticity calculations have been performed using the method described earlier for precisely the geometries studied in DFT, and the strain energies $E_{strain}(N, V)$ are shown in Table 3. These values are generally larger than the dilute limit, and increase with increasing N due the larger fraction of β'' precipitate included in the supercell.

Figure 3 compares the DFT precipitate energies, per formula unit, versus precipitate size with predictions obtained using (i) surface energy terms only (CNT(γ)) and (ii) surface energies terms plus elastic strain energy in the DFT

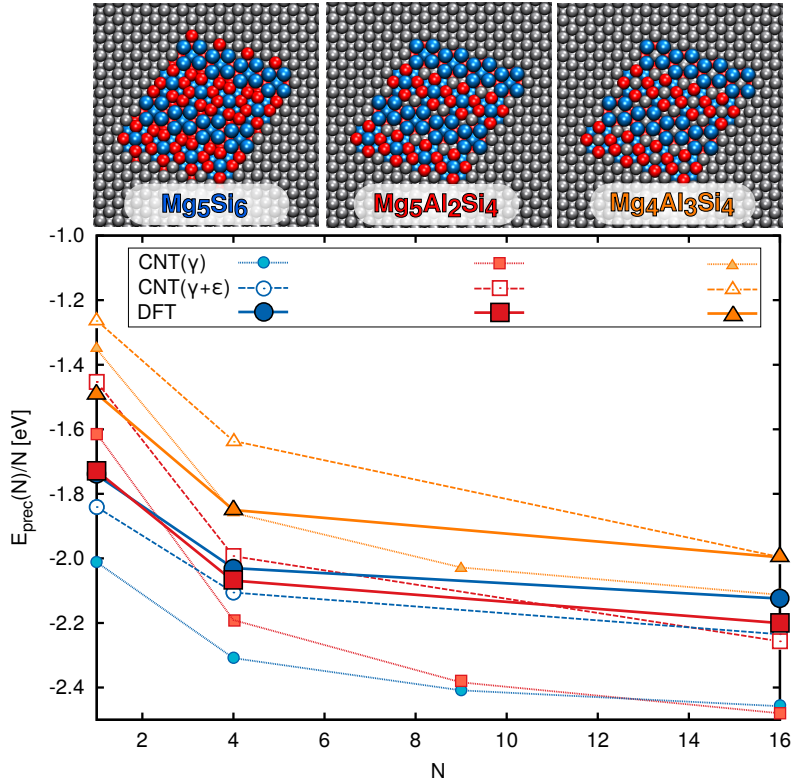


Figure 3: (Top) A view along the \mathbf{b} direction of an infinite needle-shaped β'' precipitate with 16 (4×4) formula units cross-section, embedded in a $12 \times 1 \times 12$ Al supercell for the three precipitate compositions. (Bottom) Precipitation energies per formula unit, $E_{prec}(N)/N$, calculated from explicit DFT calculations using Eqn. 11 and estimated from the thermodynamic CNT model in Eq. 5.

simulation cell (CNT($\gamma + \epsilon$)). The results generally follow the expected trend, in that larger precipitates are thermodynamically more stable due to the reduction in relative importance of the interface, edge, and corner energies with increasing size, and the energies approach the (size-independent) formation energies plus dilute-limit elastic energies for each of the three stoichiometries (Table 3). A CNT model that uses only the surface energies captures qualitatively the asymptotic behavior for different β'' compositions, as well as relative ordering. However, it under-estimates the energy of the precipitates in the large-precipitate-size limit, due to the absence of the positive contribution of the

elastic energy.

The CNT($\gamma + \epsilon$) model predicts quite accurately the energetics of the larger precipitates. However, it significantly overestimates the energy at the smaller sizes. The full DFT energies are up to 0.4eV/f.u *lower* than predicted by Eqn (12). One would normally expect that edge and corner terms would destabilize the nucleus (increase the energy) at the smaller sizes. Thus, the fact that the self-consistent energetics leads to stronger stabilization suggests that the surface energies computed assuming ideal interfaces provides only an upper-bound to the actual $\gamma^{A,B,C}$. Further relaxation (which is hindered for the larger precipitates, and for periodic surface calculations) could significantly lower the interface energy. Searching for reconstructions of the β'' ||Al interfaces with a top-down approach and using electronic structure calculations constitutes a formidable challenge. We expect that the development of machine-learning models[33] for classical inter-atomic potentials, together with Monte Carlo sampling techniques, might help elucidate this important contribution to the stability and morphology of precipitates in the Al-6000 series.

Comparison between the calculations we report here and those presented in Ref. 10 underscore the importance of accounting for elastic relaxation in this kind of simulations. While part of the discrepancy could be attributed to minor differences in the computational details, we note a general trend where the energies for the 4×4 precipitates reported by Ref. 10 are considerably lower than those for the smaller 2×2 precipitates, values – and in all cases but for Mg_5Si_6 – lower than our values. As shown in the Appendix, this trend can be understood in terms of the boundary conditions chosen for DFT calculations. Simulations in Ref. 10 allowed the supercell dimensions to relax, which underestimates the energy of the encapsulated precipitate relative to the dilute limit. In our calculations, instead, we fixed fixed the cell parameters to match the Al bulk lattice parameter, which, conversely, overestimates the energy. Use of a fixed supercell simplifies the comparison between calculations, and the definition of consistent surface energies. However, only a multi-scale analysis that includes a FE model makes it possible to compute the elastic corrections to the “dilute” limit and to

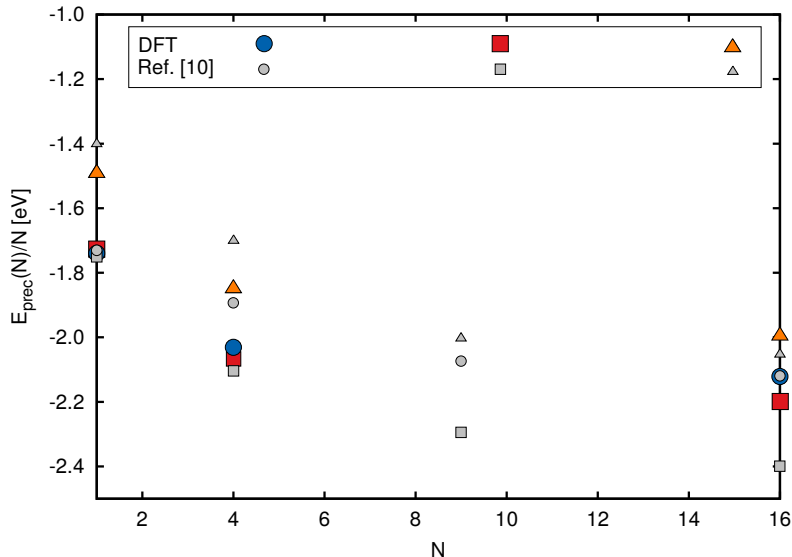


Figure 4: Precipitation energies per formula unit, $E_{prec}(N)/N$, calculated from explicit DFT calculations using Eqn. 11. Results from literature calculations that apply the same equation but include relaxation of the supercell are shown for comparison [32]. Symbols and colors are consistent with Fig. 3.

interpret quantitatively DFT results in terms of the physical contributions to the precipitate energy.

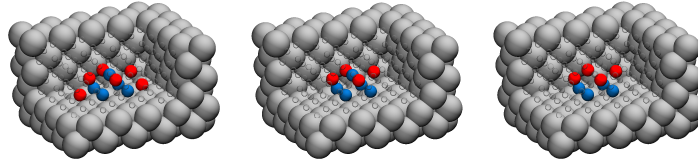
5. Nucleation of a precipitate in 3D

The analyses in the previous section show that there is no barrier for the growth of needle-like precipitates starting at the smallest size $N = 1$ for the in-plane precipitate structure. The inclusion of interface and elastic energies was essential in this analysis to verify that nanoscopic precipitates are stable despite the high interface and elastic energy contributions. We note that possible lower-energy interfaces will only enhance the stabilization of the smallest precipitates. Therefore, nucleation of all three β'' phases studied here occurs at the in-plane unit cell level or below. However, the in-plane analysis neglects the additional energy cost of the high-energy $B [010]_{\beta''}$ interface. We thus investigate here the formation energy of 3D precipitates, to better understand the precipitate

nucleation process and possible nucleation barriers.

We simulated 3D precipitates composed of a single formula unit fully-embedded in the Al matrix. As shown in Table 4, the fully-relaxed DFT energy is negative for all compositions. This confirms that precipitation is barrierless down to a single 3D formula unit even when considering the high- γ B interfaces. At this scale, the CNT(γ) model is very inaccurate, predicting positive formation energy for all the stoichiometries except Mg_5Si_6 . The elastic strain energy computation requires a full 3d analysis, and is not performed here since the elastic term would increase the energy relative to the CNT(γ) model.

It is not surprising that a mesoscopic model cannot capture the energetics of a precipitate that consists of just eleven atoms. It is however interesting that – just as for the needle-like geometry – the mesoscale model *overestimates* the energy cost associated with the precipitate-matrix interfaces, indicating that local relaxations can significantly lower the interface excess energy as compared to the ideal unreconstructed interfaces.



E_{prec} [meV]	Mg_5Si_6	$Mg_5Al_2Si_4$	$Mg_4Al_3Si_4$
DFT	-658	-558	-351
CNT(γ)	-102	513	497

Table 4: (Top) Snapshots of the simulation cells used to model single-formula-unit precipitates fully-encapsulated in the Al-matrix. (Table) Precipitation energies of one formula unit precipitates computed from DFT calculations (Eqn. (11)) and the CNT model (5) with and without the finite element strain term. The area of the different interfaces has been assumed to correspond to those of half of the monoclinic unit cell.

6. Conclusion

By clearly identifying the chemical, surface, and elastic strain energies that contribute to the total precipitation energy versus size and composition, and demonstrating that the overall trends are consistent with a thermodynamic classical-nucleation-theory-like model, we have provided new insights into the early stages of the formation of β'' precipitates in Al-6000 alloys.

The in-situ needle-like β'' precipitates are found to be stable relative to the solid solution down to the smallest in-plane formula unit, indicating barrier-less growth at and above this size. The composition dependence of the total energies is subtle, with two compositions being quite close in energy. Thus, the inclusion of surface energies and elastic energies due to the different precipitate structures and compositions is essential for interpreting the DFT results and for then determining the energetics in the more-dilute limit of real materials. The benchmarking of the CNT-type model also provides a validation for the use of such mesoscopic models in other systems.

The largest discrepancy between the thermodynamic CNT model and DFT calculations is seen for the smallest precipitates, with the *ab initio* energies being consistently much *lower* than those predicted based on surface energies computed for a coherent interface between the precipitate and the matrix. Together with the fact that the anisotropy of γ is not sufficient to justify the aspect ratio of needle-like β'' precipitates, this observation hints strongly at the need for consideration of more complex models of the interfaces of the precipitates – including variable composition and a significant degree of reconstruction – that may help reduce the interface and elastic energies and further stabilize the small precipitates.

We further show that, down to a single formula unit that is fully encapsulated in the Al matrix, the DFT energy of a nanoscale precipitate is lower than the reference supersaturated solid solution. This underscores the fact that precipitation kinetics is likely to be diffusion-limited. Aggregates of a few solute atoms that can act as vacancy traps [34] would thus slow vacancy-mediated

solute diffusion that is necessary to form larger precipitates, greatly affecting the aging times. This conclusion of dominance of diffusion-controlled aging is also consistent with recent findings that the addition of 100 ppm of Sn to Al-6061 can significantly delay aging, attributed to trapping of the quenched-in vacancies by the Sn atoms [11, 35]. Our results thus point toward the need for a systematic study of the energetics of aggregates in the GP-zone regime, and the interactions between those aggregates and vacancies and/or trace elements in the alloy to understand and fine-tune the behavior of Al-6000 alloys in the early stages of precipitation.

Acknowledgements. The authors acknowledge insightful discussion with Dr. Christophe Sigli and Dr. Timothy Warner. DG and MC acknowledge support for this work by an Industrial Research Grant funded by Constellium. TJ and WC acknowledge support for this work through a European Research Council Advanced Grant, “Predictive Computational Metallurgy”, ERC Grant agreement No. 339081 - PreCoMet.

Appendix A. Calculation of eigenstrain and stiffness tensors

The eigenstrain $\bar{\epsilon}$ is the strain required to compensate for the misfit between the matrix and precipitate lattices, i.e., the strain that deforms a formula unit of precipitate into the shape of a formula unit of undeformed matrix. Subsequently, we show how to compute $\bar{\epsilon}$ in the global frame of reference \hat{e}_x - \hat{e}_y - \hat{e}_z described in Figure 2. The formula unit geometries of the matrix and the precipitates are monoclinic cells for which the directions of \vec{c} and \vec{b} coincide but differ in the angle β and the edge lengths a, b, c . We start by determining the material frame of reference \hat{e}_α - \hat{e}_β - \hat{e}_z as it simplifies both the expression of the edge vectors $\vec{a}, \vec{b}, \vec{c}$ and, since the elastic constants reported in Table 2 are computed in that frame, is required to compute stiffness tensors in the global frame.

The basis vectors \hat{e}_β and \hat{e}_z are collinear with the formula unit cell edge vectors defined in (1), \vec{c} and \vec{b} , respectively, and the third basis vector \hat{e}_α is

chosen to complete a right-handed orthonormal basis

$$\hat{e}_\beta = \frac{\vec{c}}{c} = \frac{1}{\sqrt{10}} (-3, 1, 0)^T, \quad \hat{e}_z = \frac{\vec{b}}{b} = (0, 0, 1)^T, \quad \hat{e}_\alpha = \hat{e}_\beta \times \hat{e}_z = \frac{1}{\sqrt{10}} (1, 3, 0)^T. \quad (\text{A.1})$$

We use the basis vectors to express the edge vectors in the global frame of reference using Table 1

$$\vec{c} = c \hat{e}_\beta, \quad \vec{b} = b \hat{e}_z, \quad \vec{a} = a \left(\sin \beta \hat{e}_\alpha + \cos \beta \hat{e}_\beta \right). \quad (\text{A.2})$$

The eigenstrain $\bar{\epsilon}$ corresponds to a displacement gradient $\nabla \vec{u}$ that transforms the precipitate edge vectors into the matrix edge vectors, see Figure A.5 (left). After defining matrices composed of the edge vectors for a precipitate $\mathbf{V}_{prec} =$

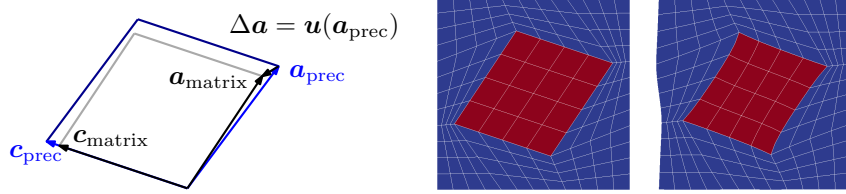


Figure A.5: Schematic illustration of eigendisplacement (left). Mesh for finite element analysis of the elastic problem (center). Note that the structured mesh follows the boundary of the precipitate (red parallelogram). Deformed elastic problem (right). The displacements have been magnified by 5 for better visibility. Note the periodic deformation.

$(\vec{a}_{prec}, \vec{b}_{prec}, \vec{c}_{prec})$ and the matrix $\mathbf{V}_{matrix} = (\vec{a}_{matrix}, \vec{b}_{matrix}, \vec{c}_{matrix})$, the displacement gradient $\nabla \vec{u}$ can be expressed as

$$\mathbf{V}_{matrix} = \nabla \vec{u} \mathbf{V}_{prec} + \mathbf{V}_{prec} \Rightarrow \nabla \vec{u} = \mathbf{V}_{matrix} \mathbf{V}_{prec}^{-1} - \mathbf{I}, \quad (\text{A.3})$$

where \mathbf{I} is the identity matrix. The eigenstrain $\bar{\epsilon}$ is the symmetric part of $\nabla \vec{u}$

$$\bar{\epsilon} = \frac{1}{2} (\nabla \vec{u} + \nabla \vec{u}^T). \quad (\text{A.4})$$

The elastic constants of the precipitates have been calculated in the material frame of reference $\hat{e}_\alpha - \hat{e}_\beta - \hat{e}_z$ and the corresponding stiffness tensor has to be rotated into the global frame of reference for the finite-element analysis. The

stress $\boldsymbol{\sigma}$ and strain $\boldsymbol{\epsilon}$ in the global frame of reference are related to the material frame stress $\boldsymbol{\sigma}'$ and strain $\boldsymbol{\epsilon}'$ by the rotation $\mathbf{R} = (\hat{e}_\alpha, \hat{e}_\beta, \hat{e}_z)$

$$\boldsymbol{\epsilon}' = \mathbf{R}\boldsymbol{\epsilon}\mathbf{R}^T, \quad \boldsymbol{\sigma}' = \mathbf{R}\boldsymbol{\sigma}\mathbf{R}^T, \quad (\text{A.5})$$

and the relationship between $\boldsymbol{\sigma}'$ and $\boldsymbol{\epsilon}'$ is governed by elasticity

$$\boldsymbol{\sigma}' = \mathbf{C}' \boldsymbol{\epsilon}', \quad (\text{A.6})$$

where \mathbf{C}' is the stiffness tensor in the material frame of reference. The stiffness tensor in the global frame of reference \mathbf{C} can be obtained by combination (A.5) and (A.6) in index notation (Einstein summation applies to repeated indices)

$$\begin{aligned} R_{ij}\sigma_{jk}R_{lk} &= C'_{ilmn}R_{mo}\epsilon_{op}R_{np}, \\ \underbrace{R_{ia}R_{ij}}_{\delta_{aj}}\sigma_{jk}\underbrace{R_{lk}R_{lb}}_{\delta_{kb}} &= R_{ia}C'_{ilmn}R_{mo}\epsilon_{op}R_{np}R_{lb}, \\ \sigma_{ab} &= R_{ia}R_{lb}C'_{ilmn}R_{mo}R_{np}\epsilon_{op}, \\ C_{abop} &= R_{ia}R_{lb}R_{mo}R_{np}C'_{ilmn}. \end{aligned} \quad (\text{A.7})$$

Appendix B. Elastic calculations

The elastic calculations use the finite element method [36] and have been performed using a modified version of the open-source finite-element code Akantu [37]. This section explains the chosen procedure.

We modeled the elastic problem using a structured, quadrilateral, and periodic two-dimensional mesh of bi-quadratic serendipity elements with eight nodes [38]. The element type was chosen over linear elements for its high accuracy in static problems. In order to enforce periodic boundary conditions, we define the boundary nodes i_s of the upper and right boundary as slave nodes to their counterparts on the bottom and left boundary (master nodes i_m). During the evaluation of nodal forces on master nodes \vec{f}_{i_m} , the forces acting their slave nodes are also assembled on the master $\vec{f}_{i_m}^{\text{tot}} = \vec{f}_{i_m} + \vec{f}_{i_s}$ and the slave node displacement is set to be equal to the displacement of their master $\vec{u}_{i_s} = \vec{u}_{i_m}$.

In order to preclude solid body motion (and, thus, a singular stiffness matrix \mathbf{K}), the center node in the precipitate is fully blocked $\vec{u}_c = \mathbf{0}$.

Figure A.5 (center and right) shows such a mesh in its original and deformed state where the displacements have been amplified by a factor five for better visibility. The structured mesh follows the boundary of the precipitate, such that any element is either of matrix material (blue) or precipitate material (red). Note the periodic deformation of the simulation cell. The precipitate is preloaded with the eigenstrain $\bar{\epsilon}$ as described in Section Appendix A and the stiffness tensors for matrix \mathbf{C}_{matrix} and precipitate and \mathbf{C}_{prec} are assigned to the blue and red elements respectively. In absence of external loads, the assembled system of equations to solve is

$$\mathbf{K}\vec{U} = \vec{0}, \quad (\text{B.1})$$

where \mathbf{K} is the assembled stiffness matrix and \vec{U} is the vector of all displacement degrees of freedom. We solve this system using the direct solver Mumps [39]. The calculation of strain energy exploits the quadrature routines of Akantu using the shape functions of the elements to evaluate the integrals in (10). Figure B.6 shows the distribution of strain energy density e_{strain} for the geometries considered using the example of $\text{Mg}_4\text{Al}_3\text{Si}_4$. A mesh that is eight times finer

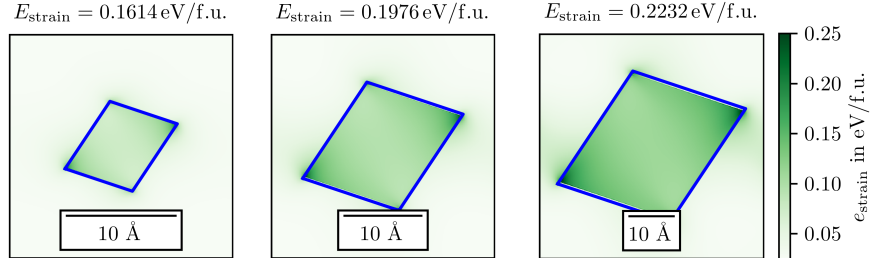


Figure B.6: Distribution of strain energy density e_{strain} for different geometries in the example of $\text{Mg}_4\text{Al}_3\text{Si}_4$. The blue frame marks the boundaries of the precipitate.

than the one represented in Figure A.5 was used for smooth visualization.

Appendix B.1. Relaxation of boundary conditions

In order to compare our results more readily to those presented in [10], we have additionally performed elastic calculations with fully relaxed periodic boundary conditions, in which the simulation box was allowed to expand and tilt as needed to have no average stress. This was done by following the procedure described in Appendix Appendix B, but with an additional uniform eigenstrain added to all elements. This additional eigenstrain was used as a degree of freedom in a minimization of the total strain energy.

Table B.5 compares the strain energies per formula unit obtained with fixed periodic boundary conditions like the ones used in all DFT calculations in this work to the energies obtained using the relaxed boundary conditions used in [10]. One can see that the relaxed conditions lead to a consistent underestimation of the strain energy, while the fixed periodic conditions lead to overestimated energies.

Composition [meV per f.u.]	dilute	4×4		2×2		1×1	
		fixed	relaxed	fixed	relaxed	fixed	relaxed
Mg ₄ Al ₃ Si ₄	74	117	53	106	59	89	66
Mg ₅ Al ₂ Si ₄	128	223	89	198	98	161	113
Mg ₅ Si ₆	140	223	114	203	122	171	132

Table B.5: Comparison of elastic strain energies E_{strain} obtained for all considered geometries with periodic boundary conditions of fixed dimensions (as the DFT calculations in this work) or fully relaxed conditions for which there is no mean stress on the simulation box (as in [10]).

References

References

- [1] M. Murayama, K. Hono, Pre-precipitate clusters and precipitation processes in AlMgSi alloys, *Acta Materialia* 47 (5) (1999) 1537–1548. doi:10.1016/S1359-6454(99)00033-6.

- URL <http://linkinghub.elsevier.com/retrieve/pii/S1359645499000336>
- [2] G. Edwards, K. Stiller, G. Dunlop, M. Couper, The precipitation sequence in AlMgSi alloys, *Acta Materialia* 46 (11) (1998) 3893–3904. doi:10.1016/S1359-6454(98)00059-7.
- URL <http://linkinghub.elsevier.com/retrieve/pii/S1359645498000597>
- [3] S. Ringer, K. Hono, Microstructural Evolution and Age Hardening in Aluminium Alloys, *Materials Characterization* 44 (1-2) (2000) 101–131. doi:10.1016/S1044-5803(99)00051-0.
- URL <http://linkinghub.elsevier.com/retrieve/pii/S1044580399000510>
- [4] C. Ravi, C. Wolverton, First-principles study of crystal structure and stability of Al/Mg/Si/(Cu) precipitates, *Acta Materialia* 52 (2004) 4213–4227.
- [5] C. D. Marioara, S. J. Andersen, H. W. Zandbergen, R. Holmestad, The influence of alloy composition on precipitates of the Al-Mg-Si system, *Metallurgical and Materials Transactions A* 36 (3) (2005) 691–702.
- URL <http://link.springer.com/article/10.1007/s11661-005-0185-1>
- [6] M. Takeda, F. Ohkubo, T. Shirai, K. Fukui, Stability of metastable phases and microstructures in the ageing process of AlMgSi ternary alloys, *Journal of materials science* 33 (9) (1998) 2385–2390.
- URL <http://link.springer.com/article/10.1023/A:1004355824857>
- [7] S. J. Andersen, H. W. Zandbergen, J. Jansen, C. Traeholt, U. Tundal, O. Reiso, The crystal structure of the β phase in AlMgSi alloys, *Acta Materialia* 46 (9) (1998) 3283–3298.
- URL <http://www.sciencedirect.com/science/article/pii/S135964549700493X>

- [8] M. W. Zandbergen, Q. Xu, A. Cerezo, G. D. W. Smith, Data analysis and other considerations concerning the study of precipitation in AlMgSi alloys by Atom Probe Tomography, *Data in Brief* 5 (2015) 626–641. doi:10.1016/j.dib.2015.09.045.
URL <http://www.sciencedirect.com/science/article/pii/S2352340915002395>
- [9] C. Marioara, S. Andersen, J. Jansen, H. Zandbergen, The influence of temperature and storage time at RT on nucleation of the phase in a 6082 AlMgSi alloy, *Acta Materialia* 51 (3) (2003) 789–796. doi:10.1016/S1359-6454(02)00470-6.
URL <http://linkinghub.elsevier.com/retrieve/pii/S1359645402004706>
- [10] P. H. Ninive, A. Strandlie, S. Gulbrandsen-Dahl, W. Lefebvre, C. D. Marioara, S. J. Andersen, J. Friis, R. Holmestad, O. M. Lrvik, Detailed atomistic insight into the phase in almgSi alloys, *Acta Materialia* 69 (2014) 126–134. doi:10.1016/j.actamat.2014.01.052.
- [11] S. Pogatscher, H. Antrekowitsch, M. Werinos, F. Moszner, S. S. A. Gerstl, M. F. Francis, W. A. Curtin, J. F. Löffler, P. J. Uggowitzer, Diffusion on Demand to Control Precipitation Aging: Application to Al-Mg-Si Alloys, *Phys. Rev. Lett.* 112 (2014) 225701.
- [12] C. D. Marioara, S. J. Andersen, J. Jansen, H. W. Zandbergen, Atomic model for GP-zones in a 6082 AlMgSi system, *Acta materialia* 49 (2) (2001) 321–328.
URL <http://www.sciencedirect.com/science/article/pii/S1359645400003025>
- [13] P. M. Derlet, S. J. Andersen, C. D. Marioara, A. Frseth, A first-principles study of the β -phase in Al-Mg-Si alloys, *Journal of Physics: Condensed Matter* 14 (15) (2002) 4011.

URL <http://iopscience.iop.org/article/10.1088/0953-8984/14/15/315/meta>

- [14] H. S. Hasting, A. G. Froseth, S. J. Andersen, R. Vissers, J. C. Walmsley, C. D. Marioara, F. Danoix, W. Lefebvre, R. Holmestad, Composition of [sup] precipitates in AlMgSi alloys by atom probe tomography and first principles calculations, *Journal of Applied Physics* 106 (12) (2009) 123527. doi:10.1063/1.3269714.

URL <http://scitation.aip.org/content/aip/journal/jap/106/12/10.1063/1.3269714>

- [15] P. Giannozzi, S. Baroni, N. Bonini, M. Calandra, R. Car, C. Cavazzoni, D. Ceresoli, G. L. Chiarotti, M. Cococcioni, I. Dabo, A. D. Corso, S. de Gironcoli, S. Fabris, G. Fratesi, R. Gebauer, U. Gerstmann, C. Gougoussis, A. Kokalj, M. Lazzeri, L. Martin-Samos, N. Marzari, F. Mauri, R. Mazzarello, S. Paolini, A. Pasquarello, L. Paulatto, C. Sbraccia, S. Scandolo, G. Sclauszero, A. P. Seitsonen, A. Smogunov, P. Umari, R. M. Wentzcovitch, QUANTUM ESPRESSO: a modular and open-source software project for quantum simulations of materials, *J. Phys. Condens. Matter* 21 (39) (2009) 395502–395519.

- [16] J. P. Perdew, K. Burke, M. Ernzerhof, Generalized Gradient Approximation made simple, *Phys. Rev. Lett.* 77 (18) (1996) 3865.

- [17] D. Vanderbilt, Soft self-consistent pseudopotentials in a generalized eigenvalue formalism, *Phys. Rev. B* 41 (1990) 7892–7895.

- [18] G. Kresse, D. Joubert, From ultrasoft pseudopotentials to the projector augmented-wave method, *Physical Review B* 59 (3) (1999) 1758.

URL <http://journals.aps.org/prb/abstract/10.1103/PhysRevB.59.1758>

- [19] I. Castelli, N. Marzari, Standard solid state pseudopotentials (2015).

URL <http://materialscloud.org/>

- [20] H. J. Monkhorst, J. D. Pack, Special points for Brillouin-zone integrations, *Phys. Rev. B* 13 (12) (1976) 5188–5192.
- [21] W. P. Davey, Precision measurements of the lattice constants of twelve common metals, *Physical Review* 25 (6) (1925) 753.
URL <http://journals.aps.org/pr/abstract/10.1103/PhysRev.25.753>
- [22] M. J. Tambe, N. Bonini, N. Marzari, Bulk aluminum at high pressure: A first-principles study, *Physical Review B* 77 (17). doi:10.1103/PhysRevB.77.172102.
URL <http://link.aps.org/doi/10.1103/PhysRevB.77.172102>
- [23] O. H. Nielsen, R. M. Martin, First-principles calculation of stress, *Physical Review Letters* 50 (9) (1983) 697.
URL <http://journals.aps.org/prl/abstract/10.1103/PhysRevLett.50.697>
- [24] G. V. Sinko, N. A. Smirnov, Ab initio calculations of elastic constants and thermodynamic properties of bcc, fcc, and hcp al crystals under pressure, *Journal of Physics: Condensed Matter* 14 (29) (2002) 6989.
URL <http://stacks.iop.org/0953-8984/14/i=29/a=301>
- [25] C. Bercegeay, S. Bernard, First-principles equations of state and elastic properties of seven metals, *Physical Review B* 72 (21). doi:10.1103/PhysRevB.72.214101.
URL <http://link.aps.org/doi/10.1103/PhysRevB.72.214101>
- [26] R. Yu, J. Zhu, H. Ye, Calculations of single-crystal elastic constants made simple, *Computer Physics Communications* 181 (3) (2010) 671–675. doi:10.1016/j.cpc.2009.11.017.
URL <http://linkinghub.elsevier.com/retrieve/pii/S0010465509003932>

- [27] D. Li, L. Chen, Computer simulation of stress-oriented nucleation and growth of precipitates in AlCu alloys, *Acta Materialia* 46 (8) (1998) 2573–2585. doi:10.1016/S1359-6454(97)00478-3.
URL <http://linkinghub.elsevier.com/retrieve/pii/S1359645497004783>
- [28] K. Luo, B. Zang, S. Fu, Y. Jiang, D.-q. Yi, Stress/strain aging mechanisms in Al alloys from first principles, *Transactions of Nonferrous Metals Society of China* 24 (7) (2014) 2130–2137. doi:10.1016/S1003-6326(14)63323-9.
URL <http://linkinghub.elsevier.com/retrieve/pii/S1003632614633239>
- [29] S. Fu, D.-q. Yi, H.-q. Liu, Y. Jiang, B. Wang, Z. Hu, Effects of external stress aging on morphology and precipitation behavior of θ phase in Al-Cu alloy, *Transactions of Nonferrous Metals Society of China* 24 (7) (2014) 2282–2288. doi:10.1016/S1003-6326(14)63345-8.
URL <http://linkinghub.elsevier.com/retrieve/pii/S1003632614633458>
- [30] J.-Y. Yao, D. A. Graham, B. Rinderer, M. J. Couper, A TEM study of precipitation in AlMgSi alloys, *Micron* 32 (8) (2001) 865–870.
URL <http://www.sciencedirect.com/science/article/pii/S0968432800000950>
- [31] Y. Wang, Z.-K. Liu, L.-Q. Chen, C. Wolverton, First-principles calculations of θ -Al interfaces, *Acta Materialia* 55 (17) (2007) 5934–5947. doi:10.1016/j.actamat.2007.06.045.
URL <http://linkinghub.elsevier.com/retrieve/pii/S1359645407004673>
- [32] P. H. Ninive, O. M. Lrvik, A. Strandlie, Density Functional Study of the θ Phase in Al-Mg-Si Alloys, *Metallurgical and Materials Transactions A* 45 (6) (2014) 2916–2924. doi:10.1007/s11661-014-2214-4.
URL <http://link.springer.com/10.1007/s11661-014-2214-4>

- [33] R. Kobayashi, D. Giofré, T. Junge, M. Ceriotti, W. A. Curtin. [link].
URL `privatecommunication`
- [34] S. Pogatscher, H. Antrekowitsch, H. Leitner, T. Ebner, P. Uggowitzer, Mechanisms controlling the artificial aging of al-mg-si alloys, *Acta Materialia* 59 (9) (2011) 3352–3363. doi:10.1016/j.actamat.2011.02.010.
URL `https://doi.org/10.1016%2Fj.actamat.2011.02.010`
- [35] M. Francis, W. Curtin, Microalloying for the controllable delay of precipitate formation in metal alloys, *Acta Materialia* 106 (2016) 117–128. doi:10.1016/j.actamat.2016.01.014.
URL `https://doi.org/10.1016%2Fj.actamat.2016.01.014`
- [36] O. C. Zienkiewicz, *The finite element method*, 3rd Edition, McGraw-Hill, London - New York, 1977.
- [37] N. Richart, J.-F. Molinari, Implementation of a parallel finite-element library: test case on a non-local continuum damage model, *Finite Elements in Analysis and Design* 100 (2015) 41–46.
- [38] J. G. Ergatoudis, *Isoparametric finite elements in two and three dimensional stress analysis.*, Ph.D. thesis, University College of Swansea (1968).
- [39] P. Amestoy, I. Duff, J.-Y. L'Excellent, *Mumps multifrontal massively parallel solver version 2.0* (1998).